THE JOURNAL OF BIOLOGICAL CHEMISTRY VOL. 291, NO. 18, pp. 9785–9795, April 29, 2016

Dimerization of Bacterial Diaminopimelate Decarboxylase Is Essential for Catalysis*

Received for publication, October 5, 2015, and in revised form, February 18, 2016 Published, JBC Papers in Press, February 26, 2016, DOI 10.1074/jbc.M115.696591

Martin G. Peverelli[‡§], **Tatiana P. Soares da Costa**[‡1], **Nigel Kirby**[¶], **and Matthew A. Perugini**[‡§2]

From the [‡]*Department of Biochemistry and Genetics, La Trobe Institute for Molecular Science, La Trobe University, Melbourne, Victoria 3086, the* [§]*Department of Biochemistry and Molecular Biology, Bio21 Molecular Science and Biotechnology Institute, Parkville, Victoria 3010, and the* [¶]*The Australian Synchrotron, 800 Blackburn Road, Clayton, Victoria 3168, Australia*

Diaminopimelate decarboxylase (DAPDC) catalyzes the final step in the diaminopimelate biosynthesis pathway of bacteria. The product of the reaction is the essential amino acid L-lysine, which is an important precursor for the synthesis of the peptidoglycan cell wall, housekeeping proteins, and virulence factors of bacteria. Accordingly, the enzyme is a promising antibacterial target. Previous structural studies demonstrate that DAPDC exists as monomers, dimers, and tetramers in the crystal state. However, the active oligomeric form has not yet been determined. We show using analytical ultracentrifugation, small angle x-ray scattering, and enzyme kinetic analyses in solution that the active form of DAPDC from *Bacillus anthracis*, *Escherichia coli*, *Mycobacterium tuberculosis*, and *Vibrio cholerae* is a dimer. The importance of dimerization was probed further by generating dimerization interface mutants (N381A and R385A) of *V. cholerae* DAPDC. Our studies indicate that N381A and R385A are significantly attenuated in catalytic activity, thus confirming that dimerization of DAPDC is essential for function. These findings provide scope for the development of new antibacterial agents that prevent DAPDC dimerization.

Diaminopimelate decarboxylase (DAPDC)[3] (E.C. 4.1.1.20) is a member of the pyridoxal 5′-phosphate (PLP)-dependent decarboxylases (1). It catalyzes the irreversible and stereospecific decarboxylation of *meso*-diaminopimelate (*meso*-DAP) in the final step of the diaminopimelate (DAP) biosynthesis pathway of bacteria and plants (2, 3). The product of the reaction, L-lysine, is an important building block for the biosynthesis of the peptidoglycan cell wall, housekeeping proteins, and virulence factors of bacteria. Consequently, DAPDC represents a promising target for the development of novel antibacterial agents (4).

A DAPDC reaction mechanism has been previously proposed (5, 6). The reaction mechanism is thought to be initiated by the formation of a Schiff base between PLP and a conserved active site lysine from the (Y/F)A*X*KA motif (7). The substrate, *meso*-DAP, then binds and forms a subsequent Schiff base with PLP. This is suggested to be coordinated by the highly conserved CE(S/T)*X*D motif provided by an adjacent subunit (7). Decarboxylation of *meso*-DAP is then mediated by the sulfhydryl nucleophile provided by the conserved cysteine of the CE(S/T)*X*D motif thereby leaving the substrate cradled between two monomers (8). This proposed mechanism suggests DAPDC functions as a dimer.

To support this assertion, previous structural studies of DAPDC from *Methanocaldococcus jannaschii* (PDB codes 1TWI and 1TUF) (9), *Aquifex aeolicus* (PDB code 2P3E), and *Brucella melitensis* (PDB code 3VAB) show that the enzyme crystallizes as a homodimer, with each monomer comprised of two domains (9). Domain I forms an α/β barrel, whereas domain II is comprised of a mixed β-sheet flanked by α-helices (9). The overall fold is similar to the functionally related enzyme ornithine decarboxylase, which also uses PLP as a cofactor in a decarboxylation of a secondary amine (10). Although the crystal structures of DAPDC from all species are shown to adopt the same tertiary fold, significant differences are observed at the quaternary level in the crystal state. For example, the asymmetric unit of DAPDC from *Escherichia coli* (PDB codes 1KNW and 1KO0) (Fig. 1*A*) (11), *Thermotoga maritima* (PDB code 2YXX), and *Helicobacter pylori* (PDB code 2QGH) (8) is a monomer; whereas DAPDC from *Vibrio cholerae* (PDB code 3N2B) adopts a tetramer (Fig. 1*B*). Interestingly, DAPDC from *Mycobacterium tuberculosis* has been crystallized as both a dimer (PDB codes 1HKW and 1HKV) (7) and a tetramer (PDB code 2O0T) (Fig. 1, *C* and *D*) (12). However, the tetrameric form observed in the asymmetric unit of DAPDC from *M. tuberculosis* (Fig. 1*D*) differs from that observed for *V. cholerae* (Fig. 1*B*).

Adding to this confusion are the results of earlier studies aimed at characterizing the quaternary structure of DAPDC in solution. Analytical ultracentrifugation analysis of *E. coli* DAPDC suggested that the enzyme exists as a 5.4 S tetramer with a molecular mass of 200 kDa (13). Although small-angle x-ray scattering (SAXS) of *M. tuberculosis* DAPDC at 9 and 18 mg ml^{-1} found it to be mostly dimeric, with the scattering data

* This work was supported in part by Australian Research Council (ARC) Discovery Project DP150103313. The authors declare that they have no conflicts of interest with the contents of this article.
[1] Supported by National Health and Medical Research Council of Australia Grant APP1091976 for fellowship support.
[2] To whom correspondence should be addressed: Dept. of Biochemistry and Genetics, La Trobe Institute for Molecular Science, La Trobe University, Melbourne, Victoria 3086, Australia. Tel.: 61-3-6479-6570; Fax: 61-3-9479-1266; E-mail: M.Perugini@latrobe.edu.au.
[3] The abbreviations used are: DAPDC, diaminopimelate decarboxylase; AUFDS, fluorescence-detected analytical ultracentrifugation; DAP, diaminopimelate; D_{max}, maximum particle size; FDS, fluorescence detection system; *P*(r), pairwise distance-distribution function; PISA, protein interfaces, surfaces and assemblies; PLP, pyridoxal 5′-phosphate; SAXS, small-angle x-ray scattering; TCEP, tris(2-carboxyethyl)phosphine; PDB, Protein Data Bank.

best represented by a mixture of 93% dimer and 7% tetramer (12).

Accordingly, we set out in this study to comprehensively characterize the quaternary structure of DAPDC in aqueous solution from different bacterial species. Given that the aforementioned kinetic mechanism proposes that active site residues are contributed by adjacent subunits, we hypothesized that DAPDC functions as a dimer in solution.

Experimental Procedures

Protein Expression and Purification of DAPDC Enzymes—DAPDC from *Bacillus anthracis* (*Ba*-DAPDC), *E. coli* (*Ec*-DAPDC), and *M. tuberculosis* (*Mt*-DAPDC) were expressed and purified as described in Peverelli and Perugini (14). Expression and purification of *V. cholerae* DAPDC (*Vc*-DAPDC) was achieved as follows. The nucleotide sequence of the *V. cholerae* DAPDC gene (*lysA*) was first identified from the Kyoto Encyclopedia of Genes and Genomes database as entry VC0125. The amino acid sequence was subsequently altered to match the amino acid sequence from PDB code 3N2B. Next, the codon-optimized nucleotide sequence was commercially synthesized by GeneArt (Life Technologies) and subcloned into the expression vector pET11a (Novagen). The vector was then transformed into *E. coli* BL21(DE3) cells and expression and purification of the recombinant enzyme was performed as previously described (14, 15).

Generation of Vc-DAPDC N381A and R385A Mutants—The QuikChange II XL site-directed mutagenesis kit (Stratagene) was employed to introduce the R385A point mutation into the *V. cholerae lysA* gene ligated into pET11a using the primer set of 5′-CAATTACAATACCCGTCCGGCTGTTGCCGAAGTTATGGTT-3′ and 5′-AACCATAACTTCGGCAACAGCCGGACGGGTATTGTAATTG-3′ (mismatched nucleotides are underlined). Mutagenesis was performed according to the manufacturer's instructions with successful mutations confirmed by dideoxynucleotide sequencing. By contrast, the N381A mutant was commercially synthesized by Bioneer and subcloned into the expression vector pET11a (Novagen). The recombinant N381A and R385A mutants were expressed and purified using the same protocol adopted for the wild-type enzyme.

Mass Spectrometry—To determine the molar mass of purified recombinant DAPDC enzymes, electrospray ionization time-of-flight mass spectrometry was performed as previously described by Hor *et al.* (16). Recombinant proteins were also subjected to trypsin digestion and the resulting tryptic fragments were sequenced by tandem mass spectrometry as reported previously (17).

Circular Dichroism (CD) Spectroscopy—CD spectroscopy was performed using an Aviv Biomedical Model 410-SF CD spectrophotometer as reported previously (16, 18–20). Samples typically consisted of 0.15 mg ml^{-1} enzyme in a buffer of 20 mM Tris, 150 mM NaCl, 1 mM Tris(2-carboxyethyl)phosphine (TCEP), pH 8.0. Spectra were measured in a 1-mm quartz cuvette between 190 and 250 nm employing a step size of 0.5 nm and 4-s averaging time. Data were analyzed using the CONTINLL algorithm and SP43 database from the CDPro software package (21).

Absorbance Detected Analytical Ultracentrifugation—Sedimentation velocity and sedimentation equilibrium experiments were performed in a Beckman XL-I analytical ultracentrifuge with a four-hole An-60 Ti or eight-hole An-50 Ti rotor at 20 °C as described previously (16, 18–20, 22, 23). The partial specific volume ($\bar{\nu}$) of the DAPDC samples together with the density and viscosity of the buffers were computed using the program SEDNTERP (24). For sedimentation velocity experiments, double sector quartz cells were loaded with 400 μl of reference (20 mM Tris, 150 mM NaCl, 1 mM TCEP, pH 8.0) and 380 μl of sample (3 μM), and data were collected at 40,000 rpm from 5.8 to 7.3 cm using a step size of 0.003 cm without averaging. Sedimentation velocity data were analyzed using the continuous size-distribution model (25, 26) employing the program SEDFIT. For sedimentation equilibrium experiments of R385A and N381A, double sector quartz cells were loaded with 140 μl of reference and 100 μl of sample (0.4–1.0 μM) with the sample sector also containing 20 μl of heavy (FC43) oil. Experiments were performed at 9,600 rpm and 14,300 rpm. When sedimentation equilibrium was attained (~24 h at each speed), data were collected from 6.7 to 7.3 cm using a 0.001-cm step size with 10 averages. The resulting dual speed sedimentation equilibrium data at multiple protein concentrations were fitted globally to various self-association models, including a monomer-dimer model (16, 23), using SEDPHAT software (27).

Fluorophore Labeling of Vc-DAPDC—Prior to labeling, 1.0 ml of *Vc*-DAPDC (7 mg ml^{-1}) was dialyzed overnight at 4 °C against 5 liters of 100 mM sodium bicarbonate, pH 8.3, 1 mM TCEP and containing 0.1 mM PLP to protect the active site lysine (Lys^{72}) from modification. 160 nmol of Alexa Fluor 488 5-tetrafluorophenyl ester (dissolved in 60 μl of dimethyl sulfoxide) was then added to the dialyzed *Vc*-DAPDC sample and the mixture was incubated at room temperature for 80 min with continuous mixing on a rocking platform. Unincorporated fluorophore was removed by Superose 12 size exclusion liquid chromatography on a 1.0 cm × 30-cm column previously equilibrated with 20 mM Tris, 150 mM NaCl, 1 mM TCEP, 0.1 mM PLP, pH 8.0. The optimized labeling procedure yielded a ratio of 1.2:1 fluorophore to *Vc*-DAPDC monomer (determined using manufacturer's instructions).

Fluorescence Detected Analytical Ultracentrifugation (AU-FDS)—Sedimentation velocity and sedimentation equilibrium experiments were performed in a Beckman XL-A analytical ultracentrifuge equipped with a fluorescence detection system (Aviv Biomedical) using Alexa Fluor 488-labeled *Vc*-DAPDC at nanomolar concentrations. For sedimentation velocity experiments, double sector cells containing sapphire windows were loaded with 400 μl of sample. Data were collected at 40,000 rpm from 5.8 to 7.3 cm at multiple photomultiplier voltages to yield ~3,000 fluorescence counts for the highest concentration in each cell. The resulting fluorescence *versus* radial data were analyzed using a continuous size distribution model (25, 26) employing SEDFIT software. For sedimentation equilibrium experiments, double sector sapphire cells were loaded with 120 μl of sample and 40 μl of heavy oil. Samples were centrifuged at 9,000 and 14,000 rpm until sedimentation equilibrium was attained (~24 h for each speed). At equilibrium, data were collected from 6.7 to 7.3 cm at multiple photomultiplier voltages to

optimize the signal-to-noise ratio and initial fluorescence counts to ~1,000. Resulting data were corrected for photomultiplier voltage differences and normalized to pseudo-absorbance values. The pseudo-absorbance profiles were then fitted to various self-association models, including a monomer-dimer model (16, 23), using SEDPHAT software (27).

Small-angle X-ray Scattering—SAXS experiments were performed on the SAXS/WAXS beamline at the Australian Synchrotron (Melbourne, Australia). Buffer and enzyme samples at multiple concentrations were loaded into 96-well plates and incubated on a temperature-controlled sample platform at 20 °C for the duration of the experiment. Scattering data of the x-ray beam were collected using a Pilatus-1 M pixel-array detector (Dectris, Switzerland). The sample-to-detector distance was 1.6 m, covering a range of momentum transfer $0.01\ \text{Å}^{-1} < q < 0.6\ \text{Å}^{-1}$ ($q = 4\pi\sin\theta/\lambda$, where 2θ is the scattering angle and $\lambda = 1.03$ Å is the x-ray wavelength). Data sets of ~20 frames covering a 2-s exposure time were collected from a sample exposed to an x-ray beam through a 1.5-mm quartz capillary. Frames were converged and buffer scattering subtracted using ScatterBrain software (Australian Synchrotron). Guinier plots and $P(r)$ distributions were produced using PRIMUS (28–31), whereas scattering fits to crystal structures were performed using CRYSOL (32). Data generated for *Ec*-DAPDC and *Vc*-DAPDC were fitted against their respective crystal structures (PDB codes 1KNW and 3N2B), whereas the data for *Mt*-DAPDC were fitted against its dimeric crystal structure (PDB code 1HKV) or the tetramer generated from the *T. maritima* DAPDC (PDB code 2YXX). Data collected on *Ba*-DAPDC were fitted against PDB code 1HKV, as *M. tuberculosis* DAPDC is the closest homolog available in the PDB. *Ab initio* models of each DAPDC enzyme were generated using DAMMIN software (available from ATSAS online) (33).

Enzyme Kinetics Assay—DAPDC enzyme kinetic assays were performed as described in Peverelli and Perugini (14). Briefly, pre-initiation mixtures comprised of 200 mM Tris buffer, pH 8.0, 0.25–40 mM DAP, 2.5 μM saccharopine dehydrogenase, 0.16 mM NADH, 1 mM TCEP, 25 mM α-ketoglutarate, and 0.1 mM PLP were incubated for 10 min at 37 °C, DAPDC (final concentration of 5–500 nM) was then added to initiate the reaction, which was monitored by measuring the decrease in absorbance at 340 nm as a function of time using a temperature-controlled Varian Cary 4000 UV-visible spectrophotometer at 37 °C. Assays were performed in triplicate and analyzed using a Michaelis-Menten kinetic model to determine the K_m for *meso*-DAP and k_{cat} as reported previously (14).

Results

PISA Analyses of DAPDC Crystal Structures—To support our hypothesis that DAPDC functions as a dimer, we first performed computational analyses of DAPDC crystal structures from *E. coli* (PDB code 1KNW), *M. tuberculosis* (PDB code 1HKV), and *V. cholerae* (PDB code 3N2B). As reported earlier, these orthologs crystallize as monomers, dimers/tetramers, and tetramers, respectively. The *in silico* analyses were performed using the Protein Interfaces, Surfaces and Assemblies (PISA) web-based server (34), which calculates the nature of interactions stabilizing protein-protein interfaces in crystal structures. The PISA algorithm can therefore aid in discriminating between interfaces resulting from crystal artifacts *versus* those that are structurally relevant (34, 35). The PISA results conducted on 1KNW, 1HKW, and 3N2B suggest the enzymes exist as dimers (Fig. 1, *E–G*). We were therefore interested in confirming these predictions by studying the quaternary structure of the enzymes in aqueous solution.

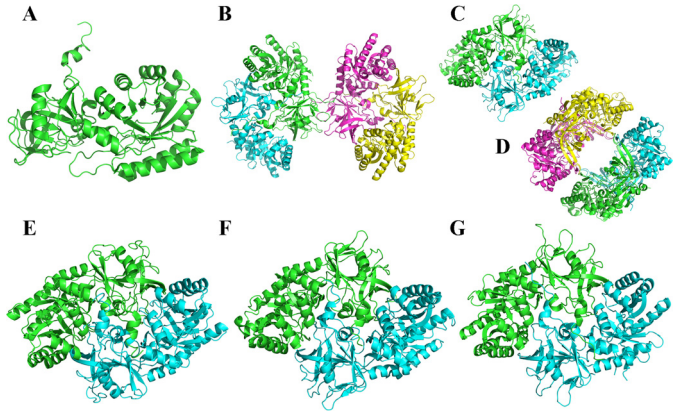

FIGURE 1. **Quaternary structure of DAPDC enzymes in the crystal form.** The asymmetric units of *A*, *Ec*-DAPDC (PDB code 1KO0); *B*, *Vc*-DAPDC (PDB code 3N2B); *C*, *Mt*-DAPDC dimer (PDB code 1HKV); and *D*, *Mt*-DAPDC tetramer (PDB code 2O0T) are displayed. The in solution assemblies calculated by PISA are shown for *E*, *Ec*-DAPDC (PDB code 1KO0), *F*, *Mt*-DAPDC (PDB code 1HKV and 2O0T); and *G*, *Vc*-DAPDC (PDB code 3N2B).

Recombinant DAPDC Enzymes Are Folded and Enzymatically Active—Before assessing and comparing the quaternary structure of *Ec*-DAPDC, *Mt*-DAPDC, and *Vc*-DAPDC, we first needed to express and purify milligram quantities of the recombinant enzymes. To expand the diversity of orthologs to also include a DAPDC from a Gram-positive bacterium, we also expressed and purified *Ba*-DAPDC. All four enzymes were produced in milligram quantities (1.69–132 mg) with >95% purity as assessed by SDS-PAGE. Mass spectrometric analyses showed that the recombinant products were comprised of the correct primary structure. CD spectroscopy studies were also performed to confirm that *Ba*-DAPDC, *Ec*-DAPDC, *Mt*-DAPDC, and *Vc*-DAPDC adopt α/β structures in solution (Table 1), consistent with x-ray crystal structure analyses (7–9, 11, 12). The enzymatic activity of the folded recombinant enzymes were next determined and compared using a recently optimized coupled assay employing saccharopine dehydrogenase (14, 36). The enzyme kinetic data for *Vc*-DAPDC is shown in Fig. 2. The resultant data fitted well to the Michaelis-Menten equation ($R^2 = 0.99$) thereby imparting a $K_m^{meso\text{-}DAP}$ of 1.9 mM, a V_{max} of 27 μmol min^{-1} mg^{-1}, and a catalytic rate constant (k_{cat}) of 22 s^{-1} (Table 2). This is similar to the kinetic parameters determined for *Ba*-DAPDC, *Ec*-DAPDC, and *Mt*-DAPDC (Table 2). We were next interested in determining the quaternary structure of the active recombinant enzymes in solution.

DAPDC Exists as a Dimer in Solution—To characterize and compare the quaternary structure of *Ba*-DAPDC, *Ec*-DAPDC, *Mt*-DAPDC, and *Vc*-DAPDC, absorbance-detected sedimentation velocity experiments were initially conducted in the analytical ultracentrifuge at a protein concentration of 150 $\mu\text{g ml}^{-1}$ (3 μM). The raw absorbance *versus* radial position data were fitted to a continuous size-distribution model yielding the $c(s)$

distributions depicted in Fig. 3. The results show that *Ba*-DAPDC and *Vc*-DAPDC exist as a monodisperse 5.6 S species (Fig. 3, *A* and *D*; Table 3). The equivalent *c*(*M*) distribution results in a single species with a modal molecular mass of 83 kDa for *Ba*-DAPDC and 92 kDa for *Vc*-DAPDC (Table 3). This suggests that the 5.6 S species is a dimer. Similarly, *Ec*-DAPDC and *Mt*-DAPDC exist primarily as a ~5.6 S species, but the *c*(*s*) distributions also show a small proportion of a ~4 S species (Fig. 3, *B* and *C*; Table 3). The *c*(*M*) distribution results for *Ec*-DAPDC and *Mt*-DAPDC indicate that the ~4 S species has a molecular mass of ~50 kDa (Table 3), suggesting that this species is a monomer. Nevertheless, the results of the sedimentation velocity experiments demonstrate that DAPDC from all four bacterial species primarily exist as dimers in aqueous solution. We therefore set out to validate these results using small-angle x-ray scattering.

SAXS Confirms DAPDC Is Dimeric—To support the initial analytical ultracentrifugation results, SAXS experiments were performed using a synchrotron x-ray source at DAPDC concentrations of 3–30 μM. The resulting scattering data were subjected to Guinier analysis (28, 29) to determine the radius of gyration (R_g) (Table 4). The maximum dimension of the scattering particle (D_{max}) for each DAPDC enzyme (Table 4) were determined from the pairwise distance-distribution function (P(r)) calculated using the indirect Fourier transform method (30). Scattering data were also evaluated using CRYSOL (32) incorporating appropriate PDB entries of DAPDC enzymes (Fig. 4; Table 4). These analyses showed that the experimental scattering profiles for *Ba*-DAPDC, *Ec*-DAPDC, and *Vc*-DAPDC best fit to the theoretical scattering profile of a dimer (Fig. 4, *A*, *B*, and *D*). However, the scattering data for *Mt*-DAPDC fit best to a dimer at 3 μM, but to a tetramer at 30 μM (Fig. 4*C*), which is consistent with previous studies (12). Furthermore, *ab initio* bead models were created using DAMMIN (33) to establish shape envelopes from the scattering data of each DAPDC sample. Crystal structures were overlaid with the bead models as shown in Fig. 4 (*insets*). Consistent with the CRYSOL results, the *ab initio* models exhibit shape envelopes that correspond to dimers for *Ba*-DAPDC, *Ec*-DAPDC, and *Vc*-DAPDC (Fig. 4, *A*, *B*, and *D*). Whereas, the bead models for *Mt*-DAPDC generated from the lowest (3 μM) and highest (30 μM) concentration datasets displayed a dimeric and tetrameric shape envelope, respectively (Fig. 4*C*). The bead models provide further evidence that the structurally relevant quaternary structure of DAPDC is a dimer. We were thus interested in further probing the relationship between the dimeric structure and enzyme function. To do this, we decided to create mutant forms of *Vc*-DAPDC with attenuated dimerization propensity and compare the catalytic activity of the mutants to the wild-type dimer. Nevertheless, it was important to first determine the dimerization affinity of wild-type *Vc*-DAPDC to enable comparison with dimer attenuated mutant forms.

AU-FDS Studies of Vc-DAPDC—Although the initial sedimentation velocity studies outlined earlier indicate that *Vc*-DAPDC exists as a stable dimer at a concentration of 3 μM (Fig. 3*D*); we set out to examine the concentration dependence of *Vc*-DAPDC dimerization by diluting the enzyme concentration by 5-fold to 30 μg ml^{-1} (0.6 μM) (Fig. 5*A*). However, no significant dissociation of the dimer was observed. This indicated

TABLE 1
Secondary structure of recombinant and mutant DAPDC enzymes
CD data were analyzed using CDPro (21) with the CONTINLL algorithm and the SP43 reference database.

DAPDC	α-Helix	β-Sheet	Turn	Random	R.m.s. deviation[a]
		%			
B. anthracis	26	21	21	32	0.09
E. coli	25	24	22	29	0.05
M. tuberculosis	24	25	21	30	0.10
V. cholerae	27	24	21	28	0.08
N381A	26	24	20	30	0.04
R385A	30	20	21	29	0.07

[a] R.m.s. deviation, root mean square deviation.

TABLE 2
Catalytic parameters of recombinant DAPDC enzymes

DAPDC	$K_m^{meso\text{-}DAP}$	k_{cat}	V_{max}	Specific activity
	mM	s^{-1}	units mg^{-1}	
B. anthracis	0.68	58	72	69
E. coli	0.97	55	70	66
M. tuberculosis	1.6	28	34	32
V. cholerae	1.9	22	27	24
V. cholerae (FDS)	ND[a]	ND	ND	22
N381A	ND	ND	ND	3.2
R385A	ND	ND	ND	1.9

[a] ND, not determined.

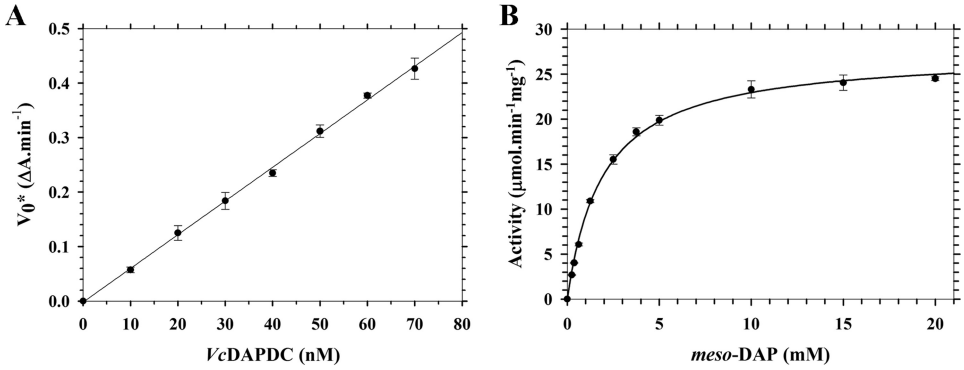

FIGURE 2. **Enzyme kinetic analysis of *Vc*-DAPDC.** The catalytic activity of *Vc*-DAPDC was investigated using the DAPDC-SDH coupled assay (14, 36). *Solid circles* represent the mean of triplicate measurements and *error bars* represent the standard deviation. *A*, a rate *versus* enzyme concentration profile. The *solid line* represents the fit to a simple linear regression model. *B*, activity of *Vc*-DAPDC plotted as a function of substrate (*meso*-DAP) concentration. The *solid line* represents the data fitted to the Michaelis-Menten equation.

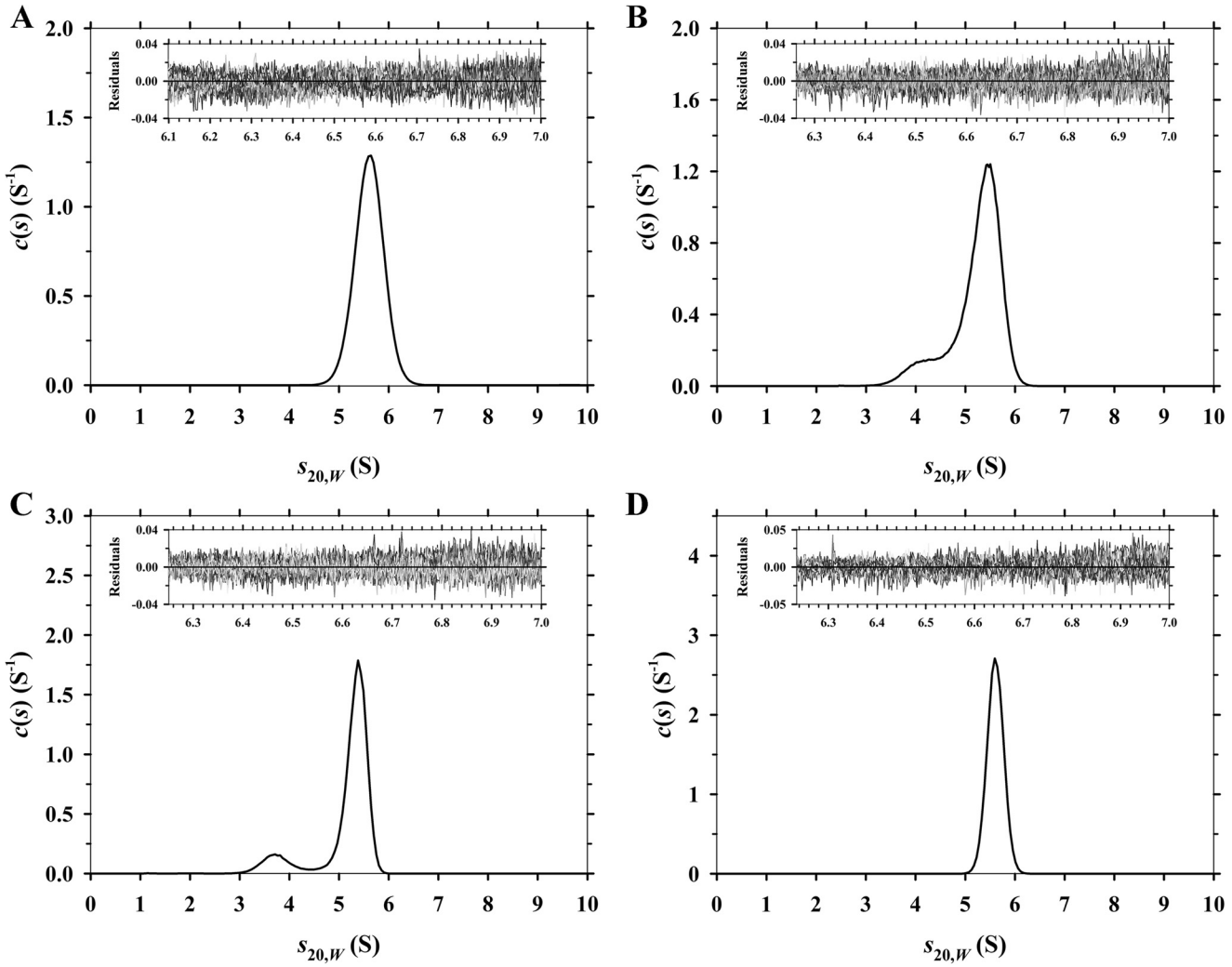

FIGURE 3. **Sedimentation velocity analysis of DAPDC enzymes.** Continuous sedimentation coefficient (*c*(*s*)) distributions plotted as a function of standardized sedimentation coefficient ($s_{20,w}$) in units of Svedberg (S). *A*, *Ba*-DAPDC; *B*, *Ec*-DAPDC; *C*, *Mt*-DAPDC; and *D*, *Vc*-DAPDC. Residuals for each experiment are displayed as *insets*.

TABLE 3
Summary of hydrodynamic properties of DAPDC enzymes

DAPDC	Oligomer	Theoretical molecular mass[a]	$s_{20,w}$	Experimental molecular mass[b]	f/f_0[c]	K_D 2→1[d]
		kDa	*S*	*kDa*		*nM*
B. anthracis	Dimer	98	5.6	83	1.3	ND[e]
E. coli	Monomer	47	4.2	52	1.1	ND
	Dimer	94	5.5	81	1.4	
M. tuberculosis	Monomer	50	3.7	50	1.3	ND
	Dimer	100	5.4	86	1.4	
V. cholerae	Dimer	98	5.6	92	1.3	ND
V. cholerae labeled (Abs)	Dimer	100	5.8	98	1.3	ND
V. cholerae	Monomer	50	3.6	41	1.3	0.06
labeled (FDS)	Dimer	100	5.6	91	1.3	
N381A	Monomer	49	3.6	46	1.2	17.3
	Dimer	98	5.1	76	1.4	
R385A	Monomer	49	3.7	51	1.2	410
	dimer	98	5.2	77	1.4	

[a] Molecular masses derived from amino acid sequence.
[b] Molecular masses obtained from the ordinate maximum of peaks in the *c*(*M*) distribution.
[c] Frictional ratio derived using the $\bar{\nu}$ bar method (24).
[d] Determined from global nonlinear best fit to a monomer-dimer equilibrium model using sedimentation equilibrium data at multiple concentrations and rotor speeds.
[e] ND, not determined.

TABLE 4
Summary of SAXS results of recombinant DAPDC enzymes

DAPDC	Concentration	Data R_g	D_{max}	χ *vs* PDB[a]	Fit R_g	PDB D_{max}
	mg ml^{-1}	*Å*				*Å*
B. anthracis	0.84	29.7 ± 0.1[b]	100	0.715	29.5	102
	0.42	30.0 ± 0.2	100	0.599	29.5	
	0.21	29.9 ± 0.3	103	0.553	29.5	
E. coli	0.50	29.5 ± 0.2	103	0.677	28.9	96.8
	0.25	29.6 ± 0.2	104	0.615	28.8	
	0.13	29.6 ± 0.8	104	0.549	28.6	
M. tuberculosis	1.4	36.5 ± 0.1	117	2.14	35.8	111
	0.70	35.8 ± 0.2	120	0.848	35.0	
	0.35	35.1 ± 0.3	115	0.878	34.7	
	0.17	34.9 ± 0.6	117	0.855	34.7	
V. cholerae	1.5	30.5 ± 0.1	107	1.70	30.6	98.5
	0.74	30.5 ± 0.1	107	0.947	30.5	
	0.37	30.4 ± 0.3	104	0.667	30.6	
	0.19	30.9 ± 1.0	113	0.601	30.6	

[a] Experimental data were fitted to theoretical scattering profiles generated from appropriate atomic coordinates using the program CRYSOL (32).
[b] Errors are estimated automatically with the help of a polynomial smoothing procedure (32).

that the dimerization dissociation constant was considerably tighter than 0.6 μM. Accordingly, a more sensitive method for detection was required and thus *Vc*-DAPDC was labeled with Alexa Fluor 488 to facilitate sedimentation studies via AU-FDS at submicromolar concentrations. Initially, absorbance-detected sedimentation velocity studies were performed on the fluorescently labeled enzyme to ensure that labeling did not

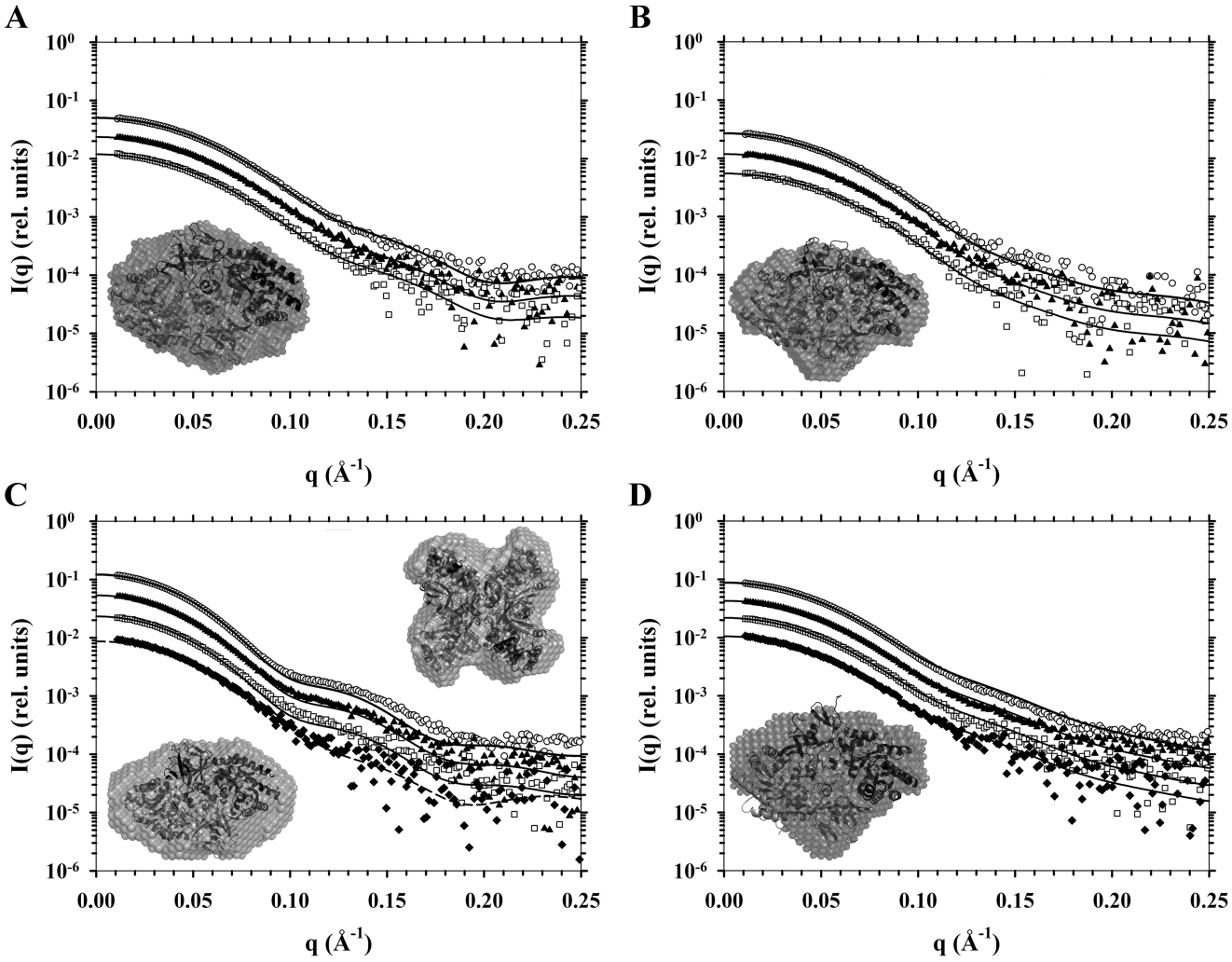

FIGURE 4. **SAXS analyses of DAPDC enzymes.** Scattering intensity in relative units is plotted as a function of momentum transfer in Å^{-1}. Buffer corrected scattering data were fitted to theoretical scattering profiles (*solid* or *dashed lines*) generated from atomic coordinates from PDB files. Data from highest to lowest concentrations are, respectively, represented by *open circles* (○), *solid triangles* (▲), *open squares* (□), and if so required *closed diamonds* (♦). Included as *insets* are DAMMIN *ab initio* bead models generated from scattering data with overlaid cartoon crystals structures. *A*, *Ba*-DAPDC scattering data from 0.84, 0.42, and 0.21 mg ml^{-1} samples and a DAMMIN bead model fitted to the *Mt*-DAPDC dimer (PDB code 1HKV). *B*, *Ec*-DAPDC scattering data from 0.50, 0.25, and 0.13 mg ml^{-1} samples and a DAMMIN bead model fitted to the dimer assembly calculated by PISA of the *E. coli* DAPDC crystal structure (PDB code 1KO0). *C*, *Mt*-DAPDC scattering data from 1.40, 0.70, 0.35, and 0.17 mg ml^{-1} samples and DAMMIN bead models fitted to either its dimer (PDB code 1HKV) or the PISA tetramer assembly generated from the *T. maritima* DAPDC crystal structure (PDB code 2YXX). *Solid lines* are fits to the 2YXX tetramer and the *dashed line* is the fit to the 1HKV dimer. *D*, *Vc*-DAPDC scattering data from 1.48, 0.74, 0.37, and 0.19 mg ml^{-1} samples and a DAMMIN bead model fitted to the dimer of PDB code 3N2B (*i.e.* chains A and B).

perturb dimerization. At 150 μg ml^{-1}, the labeled enzyme sedimented as a single species with an $s_{20,w}$ value of 5.8 S (Fig. 5*B*) and a molecular mass of 98 kDa, consistent with the unlabeled enzyme (Fig. 3*D*; Table 3). Sedimentation velocity experiments were thus performed in AU-FDS using 5 nM fluorescently labeled enzyme. The resulting continuous size distribution shows evidence of dissociation of the 5.6 S dimer to a 3.6 S monomer (Fig. 5*C*; Table 3). Importantly, we also determined that the specific activity of the Alexa Fluor 488-labeled enzyme was 22.4 units mg^{-1}, which is similar to the unlabeled enzyme (Fig. 5*D*; Table 2). This demonstrates that labeling did not significantly alter the catalytic function of *Vc*-DAPDC.

To quantify the dimerization affinity of Alexa Fluor 488-labeled *Vc*-DAPDC, sedimentation equilibrium experiments were conducted at two rotor speeds (9,000 and 14,000 rpm) and four enzyme concentrations (2, 4, 20, and 40 nM). The resulting data were globally fitted to various self-association models, including monomer-dimer, monomer-trimer, monomer-tetramer, and dimer-tetramer. The global nonlinear best fit resulted to a monomer-dimer model, which yielded a dimer-monomer dissociation constant ($K_D^{2\rightarrow1}$) of 0.061 nM (Fig. 6; Table 3). This is very tight, therefore supporting the hypothesis that dimerization is critical for DAPDC function. We next set out to design dimerization attenuation mutants to compare with the wild-type *Vc*-DAPDC dimer.

Dimer Interface Mutants Are Attenuated in Dimerization Propensity and Catalytic Activity—There are several residues that facilitate subunit interactions at the dimerization interface of *Vc*-DAPDC. This includes Arg^{385}, which forms a hydrogen bond with Asn^{379} on the adjacent subunit (Fig. 7*A*). We therefore decided to mutate Arg^{385} to an Ala in an attempt to create a dimerization attenuated mutant. Suc-

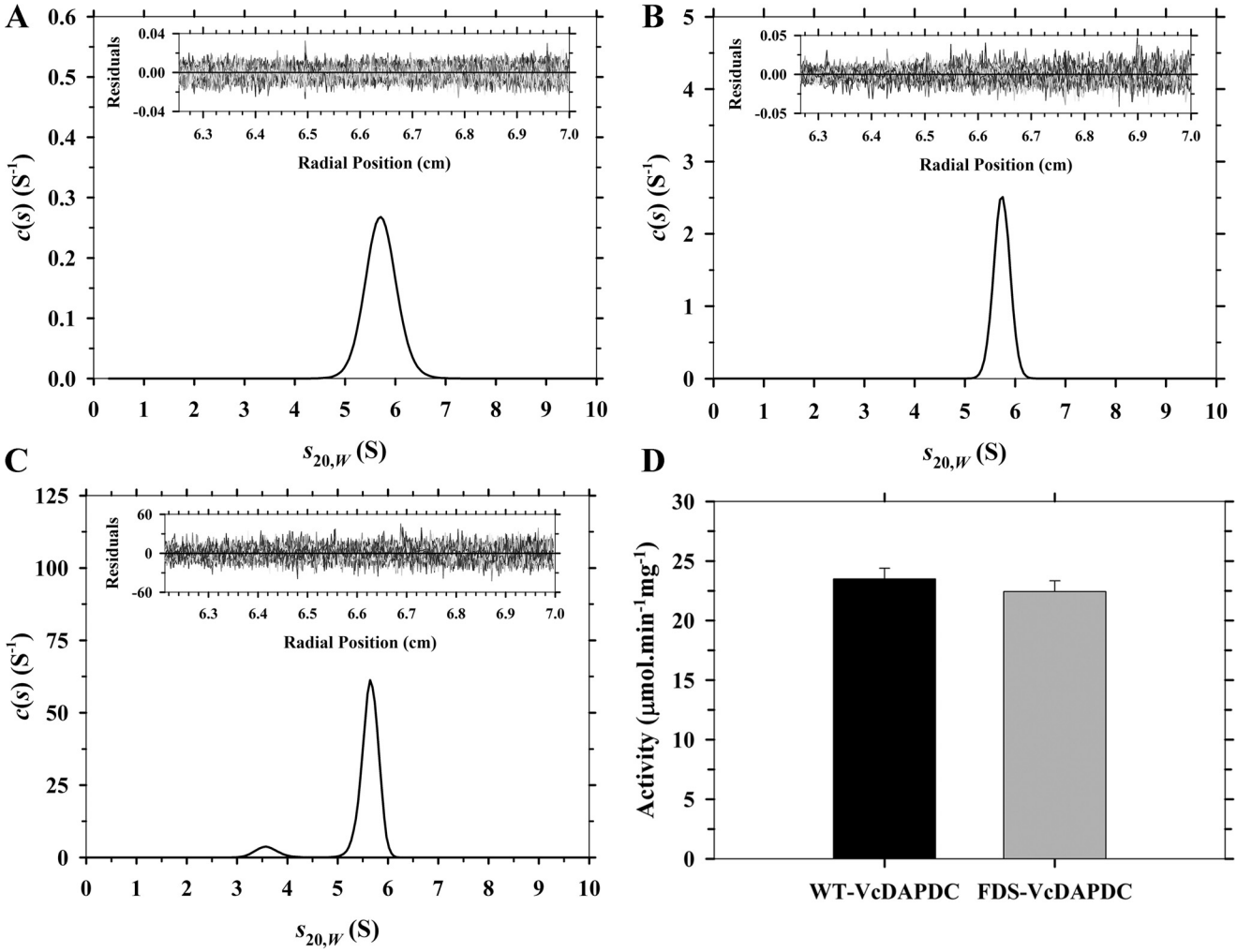

FIGURE 5. **Comparison of fluorescently labeled and unlabeled *Vc*-DAPDC.** *A–C*, continuous sedimentation coefficient (*c*(*s*)) distributions plotted as a function of standardized sedimentation coefficients ($s_{20,w}$) with residuals of fits as *insets*. *A*, *Vc*-DAPDC at 30 μg ml^{-1} (~600 nM); *B*, fluorescently labeled *Vc*-DAPDC at 150 μg ml^{-1} (~3,010 nM); and *C*, fluorescently labeled *Vc*-DAPDC at 0.25 μg ml^{-1} (5 nM). AU-FDS technique was used for *C*. *D*, comparison of wild-type *Vc*-DAPDC (WT-VcDAPDC) and fluorescently tagged *Vc*-DAPDC (FDS-VcDAPDC) specific activity at a fixed concentration of 100 nM. *Error bars* represent the standard deviation of triplicate measurements.

cessful implementation of the point mutation R385A was confirmed by dideoxynucleotide sequencing and mass spectrometry. The structure of R385A was analyzed by CD spectroscopy, which demonstrates that the point mutation did not perturb the secondary structure of the enzyme relative to wild-type *Vc*-DAPDC (Table 1).

Next, the quaternary structure of R385A was investigated using analytical ultracentrifugation. Sedimentation velocity experiments were performed over a concentration range of 0.4–20 μM. At 0.4 μM, the continuous size distribution analysis showed that the enzyme exists in a monomer-dimer equilibrium with similar proportions of each species (Fig. 7*B*; Table 3). This suggests the dimerization dissociation constant of R385A is ~400 nM. To better quantify the dimerization affinity of R385A, sedimentation equilibrium experiments were performed at two rotor speeds (9,600 and 14,300 rpm) and multiple protein concentrations (400, 600, and 1,000 nM). The resulting data were fitted to a monomer-dimer self-association model, which yielded a $K_D{}^{2\rightarrow1}$ of 0.41 μM consistent with the sedimentation velocity results (Fig. 7, *D–F*; Table 3). This indicates that dimerization of the R385A mutant is ~6,660-fold weaker than wild-type *Vc*-DAPDC.

The catalytic activity of R385A was next examined and compared with the wild-type enzyme. At a fixed concentration of 100 nM, the specific activity of R385A is 1.9 units mg^{-1}, which is ~8% of the wild-type enzyme. These results demonstrate that the wild-type *Vc*-DAPDC dimer is considerably more active than the dimer attenuated R385A mutant. Furthermore, the point mutant does not display a linear relationship between rate and enzyme concentrations (Fig. 7*C*). A distinct upward curvature is observed between 5 and 500 nM, which is indicative of a self-associating enzyme where the lower order species is significantly less active than the higher order oligomer (16, 20, 23). By contrast, the wild-type enzyme displays a linear rate *versus* concentration relationship at concentrations (5–50 nM) well above the $K_D{}^{2\rightarrow1}$ (Fig. 7*C*).

To further validate that loss of catalytic function correlates with attenuation in dimerization, a second dimer interface mutant (N381A) was cloned, expressed, purified, and characterized in solution (Tables 1–3; Fig. 7, *B* and *C*). Asn^{381} is posi-

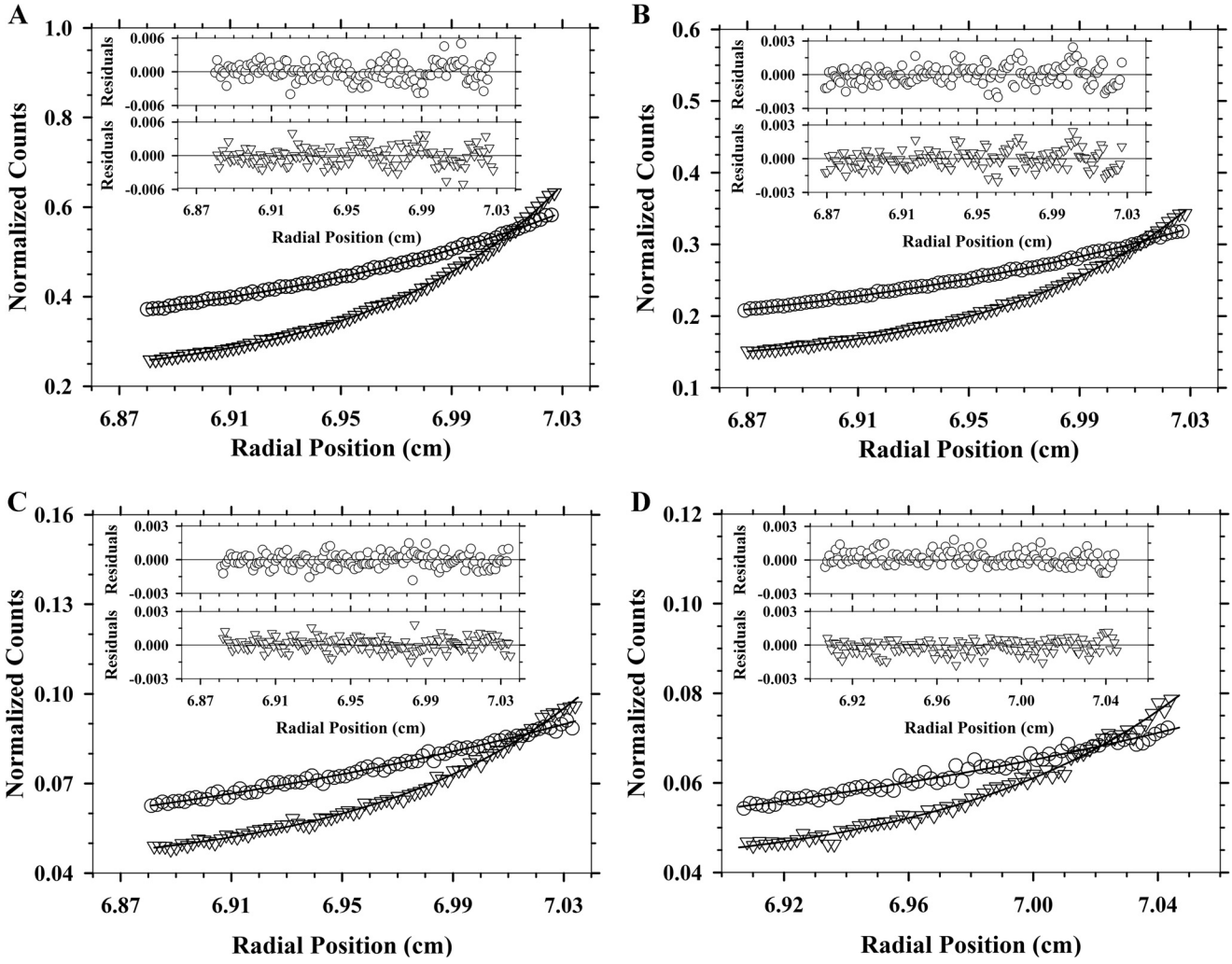

FIGURE 6. **AU-FDS sedimentation equilibrium analysis of *Vc*-DAPDC.** Once sedimentation of samples were at equilibrium at 9,000 (○) and 14,000 (▽) rpm, fluorescence emission readings of Alexa Fluor 488 from 519 nm were collected, corrected for photomultiplier voltage differences, and finally normalized to pseudo-absorbance values (*y* axes) for use in the program SEDPHAT. Overlaid to the experimental data are the global nonlinear regression best fit to a monomer-dimer self-association model (global reduced $\chi^2 = 0.039$). Residuals are displayed *above* each plot for 9,000 (○) and 14,000 (▽) rpm data. The $K_D^{2\rightarrow1}$ of 0.061 nM was yielded from experimental *Vc*-DAPDC concentrations of *A*, 40; *B*, 20; *C*, 4; and *D*, 2 nM.

tioned at the dimer interface ~10 Å from Arg^{385}, and forms an inter-chain hydrogen bond with Glu^{86}. Although less pronounced than the R385A mutant, the results show that N381A is also attenuated in dimerization propensity (Fig. 7*B*; Table 3) and catalytic activity (Fig. 7*C*). Indeed, comparison of the structure-activity properties of wild-type *Vc*-DAPDC, N381A, and R385A shows that specific activity (Table 2) correlates with dimerization affinity (*i.e.* decreasing $K_D^{2\rightarrow1}$) (Table 3).

Discussion

Given that the catalytic mechanism proposed for DAPDC assumes the enzyme exists as a dimer (7–9, 12), it is interesting to note that previous studies have not yet established whether the enzyme functions as a dimer in solution. Although the crystal structure of DAPDC from some species suggests the enzyme exists as a dimer, monomeric and tetrameric asymmetric units are also observed in the crystal state for several DAPDC structures. Nevertheless, we hypothesized that DAPDC functions as a dimer and therefore non-dimeric forms observed in the crystalline state are artifacts of crystallization or simply represent the asymmetric unit. Accordingly, the overall aim of this study was to characterize the quaternary structure of DAPDC from different bacterial species in aqueous solution.

Consistent with our hypothesis, we show using analytical ultracentrifugation, SAXS, and enzyme kinetics that DAPDC from *B. anthracis*, *E. coli*, *M. tuberculosis,* and *V. cholerae* are functional dimers in solution. These results offer strong support to the proposed catalytic mechanism implicating an essential role for dimerization for DAPDC function (7–9, 12). Moreover, the critical CE(S/T)*X*D motif required for catalysis is provided by the adjacent subunit in the dimeric complex. Dimerization has also been shown to be critical for other family members of the PLP-dependent decarboxylases, such as eukaryotic ornithine decarboxylase, where the active site is completed by the contribution of Lys^{69} and Cys^{360} from opposing subunits (10, 37). These are equivalent to the DAPDC Lys and Cys residues in the respective (Y/F)A*X*KA and CE(S/T)*X*D motifs. Mutation of these residues in mouse ornithine decarboxylase leads to heavily attenuated activity (38, 39). Clearly, these cross-interface interactions are highly important.

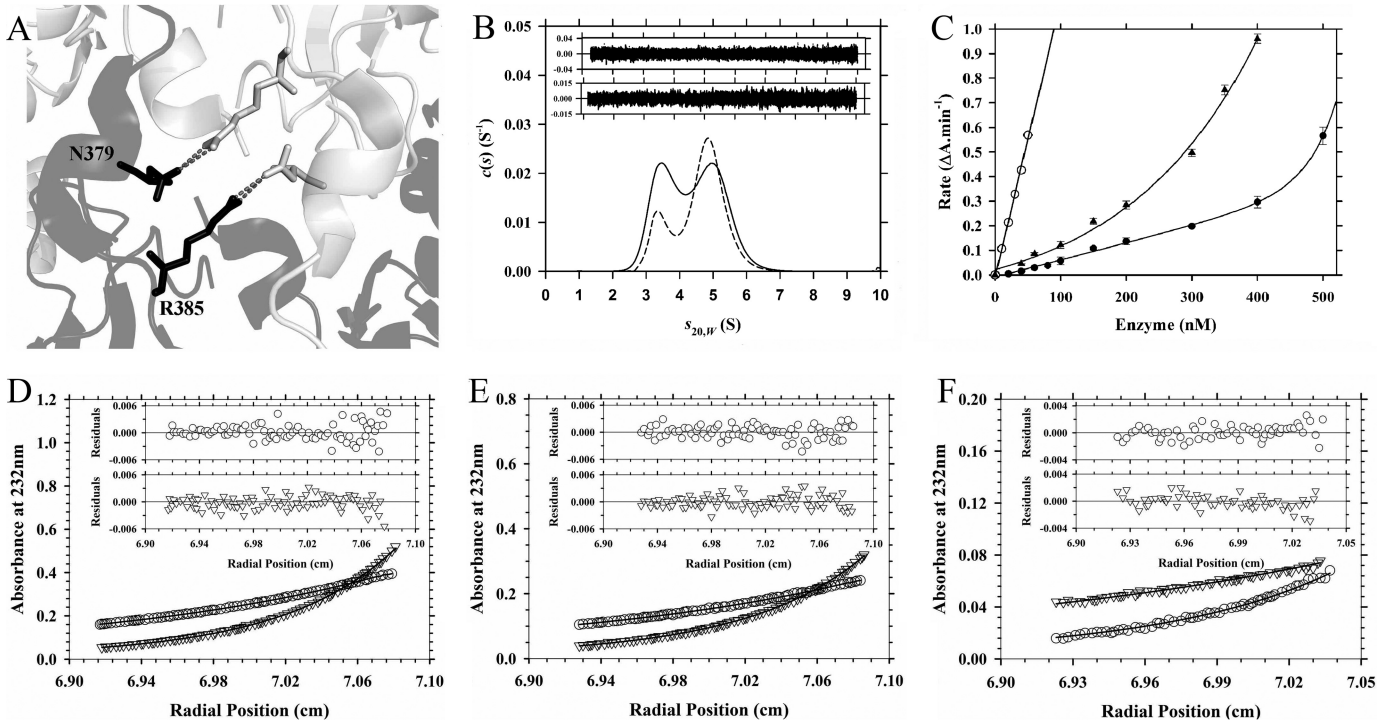

FIGURE 7. **Characterization of *Vc*-DAPDC dimer interface point mutants.** *A*, adjacent schematic chains of *Vc*-DAPDC are shown in *black* and *light gray*. In stick representation are the residues Arg^{385} (targeted for the R385A mutation) and Asp^{379}, with *gray dashed lines* representing hydrogen bond formation across the dimer interface. *B*, continuous sedimentation coefficient (*c*(*s*)) distribution plotted as a function of standardized sedimentation coefficient ($s_{20,w}$) for R385A (*solid line*) and N381A (*dashed line*) at an initial concentration of 400 nM. The residuals for the fits are displayed as an *inset* for N381A (*top*) and R385A (*bottom*). *C*, a rate *versus* enzyme concentration profile was generated for wild-type *Vc*-DAPDC (○), N381A (▲), and R385A (●). *Vc*-DAPDC data fits to a simple linear regression model. N381A and R385A data fit to a nonlinear regression model encompassing exponential growth. *Error bars* represent the standard deviation of triplicate measurements. *D–F*, absorbance at 232 nm from sedimentation equilibrium experiments were collected at 9,600 (○) and 14,300 (▽) rpm for R385A. The global nonlinear regression best fit (*solid lines*) to the monomer-dimer self-association model (global reduced $\chi^2 = 0.079$) are shown. Residuals are displayed *above* each plot for 9,600 (○) and 14,300 (▽) rpm data. The $K_D^{2\rightarrow1}$ of 0.41 μM was yielded from experimental R385A concentrations of *D*, 1,000; *E*, 600; and *F*, 400 nM.

Interestingly, these interactions are also observed for several other enzymes, including dihydrodipicolinate synthase, which catalyzes the first committed and rate-limiting step in the DAP biosynthesis pathway (2, 3). For dihydrodipicolinate synthase, dimerization has been shown to be important for completing the active site of each monomer through the interdigitation of a key catalytic triad residue (18, 20, 22, 23, 35, 40). Similarly, recent studies demonstrate that dimerization is required for the catalytic activity of diaminopimelate epimerase, which also functions in the DAP pathway (16). Additionally, dimerization has been proposed to be required for reorientating the active site in the activation of apoptotic initiator caspase 9 (41). Indeed, it is predicted that oligomerization is critical for providing key active site determinants in ~1 in 6 enzymes (42). The importance of enzyme oligomerization is therefore not always pertinent for evolving allosteric regulation sites, because more and more examples of the role of quaternary structure for the completion of active sites are being discovered. One such example is reported in this study.

Protein-protein interfaces represent highly specific drug targets, as conservation is much higher in active sites relative to interfaces. Given the increase in drug-resistant bacteria associated with the overuse and misuse of broad spectrum antibacterials, exploiting the dimerization interface of DAPDC may provide a means to negate the incidence of broad spectrum drug resistance (2, 3, 43–45).

In conclusion, we show that DAPDC from multiple bacterial species form dimers in solution and that self-association is required for activity. Consequently, preventing dimerization of DAPDC may provide a viable approach for inhibition and subsequent discovery of new antibacterial agents.

Author Contributions—M. A. P. conceived the project; M. G. P. and M. A. P. designed the majority of the experiments and co-wrote the manuscript; M. G. P. and T. P. S. C. performed the experiments and analyzed the data; N. K. co-designed, co-performed, and assisted M. G. P. with the analysis of the SAXS experiments.

Acknowledgments—We thank Dr. Manfred S. Weiss (Helmholtz Centre for Materials and Energy, Berlin) for generously providing us with the plasmid for M. tuberculosis DAPDC and Prof. Paul F. Cook (University of Oklahoma) for providing us with the plasmid for Saccharomyces cerevisiae saccharopine dehydrogenase. Part of this research was undertaken on the SAXS/WAXS beamline at the Australian Synchrotron, Victoria, Australia, and we acknowledge the La Trobe University-Comprehensive Proteomics Platform (LTU-CPP) for access to essential equipment employed in this study.

References

1. Dewey, D. L., and Work, E. (1952) Diaminopimelic acid and lysine: diaminopimelic acid decarboxylase. *Nature* **169,** 533–534
2. Dogovski, C., Atkinson, S. C., Dommaraju, S. R., Hor, L., Dobson, R. C. J., Hutton C. A., Gerrard, J. A., and Perugini, M. A. (2009) in *Biotechnology*

(Doelle, H. W., and Rokem, S., eds) pp. 116–136, Eolss Publishers, Oxford, UK
3. Dogovski, C., Atkinson, S. C., Dommaraju, S. R., Downton, M., Hor, L., Moore, S., Paxman, J. J., Peverelli, M. G., Qiu, T. W., Reumann, M., Siddiqui, T., Taylor, N. L., Wagner, J., Wubben, J. M., and Perugini, M. A. (2012) in *Biochemistry* (Ekinci, D., ed) pp. 225–262, InTech Open Access Publisher, Rijeka, Croatia
4. Hutton, C. A., Southwood, T. J., and Turner, J. J. (2003) Inhibitors of lysine biosynthesis as antibacterial agents. *Mini Rev. Med. Chem.* **3,** 115–127
5. Asada, Y., Tanizawa, K., Sawada, S., Suzuki, T., Misono, H., and Soda, K. (1981) Stereochemistry of *meso*-α,ε-diaminopimelate decarboxylase reaction: the first evidence for pyridoxal 5′-phosphate dependent decarboxylation with inversion of configuration. *Biochemistry* **20,** 6881–6886
6. Kelland, J. G., Palcic, M. M., Pickard, M. A., and Vederas, J. C. (1985) Stereochemistry of lysine formation by *meso*-diaminopimelate decarboxylase from wheat germ: use of ^{1}H-^{13}C NMR shift correlation to detect stereospecific deuterium labeling. *Biochemistry* **24,** 3263–3267
7. Gokulan, K., Rupp, B., Pavelka, M. S., Jr., Jacobs, W. R., Jr., and Sacchettini, J. C. (2003) Crystal structure of *Mycobacterium tuberculosis* diaminopimelate decarboxylase, an essential enzyme in bacterial lysine biosynthesis. *J. Biol. Chem.* **278,** 18588–18596
8. Hu, T., Wu, D., Chen, J., Ding, J., Jiang, H., and Shen, X. (2008) The catalytic intermediate stabilized by a "down" active site loop for diaminopimelate decarboxylase from *Helicobacter pylori*. *J. Biol. Chem.* **283,** 21284–21293
9. Ray, S. S., Bonanno, J. B., Rajashankar, K. R., Pinho, M. G., He, G., De Lencastre, H., Tomasz, A., and Burley, S. K. (2002) Cocrystal structures of diaminopimelate decarboxylase: mechanism, evolution, and inhibition of an antibiotic resistance accessory factor. *Structure* **10,** 1499–1508
10. Osterman, A., Grishin, N. V., Kinch, L. N., and Phillips, M. A. (1994) Formation of functional cross-species heterodimers of ornithine decarboxylase. *Biochemistry* **33,** 13662–13667
11. Momany, C., Levdikov, V., Blagova, L., and Crews, K. (2002) Crystallization of diaminopimelate decarboxylase from *Escherichia coli*, a stereospecific D-amino-acid decarboxylase. *Acta Crystallogr. D Biol. Crystallogr.* **58,** 549–552
12. Weyand, S., Kefala, G., Svergun, D. I., and Weiss, M. S. (2009) The three-dimensional structure of diaminopimelate decarboxylase from *Mycobacterium tuberculosis* reveals a tetrameric enzyme organization. *J. Struct. Funct. Genomics* **10,** 209–217
13. White, P. J., and Kelly, B. (1965) Purification and properties of diaminopimelate decarboxylase from *Escherichia coli*. *Biochem. J.* **96,** 75–84
14. Peverelli, M. G., and Perugini, M. A. (2015) An optimized coupled assay for quantifying diaminopimelate decarboxylase activity. *Biochimie* **115,** 78–85
15. Hor, L., Peverelli, M. G., Perugini, M. A., and Hutton, C. A. (2013) A new robust kinetic assay for DAP epimerase activity. *Biochimie* **95,** 1949–1953
16. Hor, L., Dobson, R. C., Downton, M. T., Wagner, J., Hutton, C. A., and Perugini, M. A. (2013) Dimerization of bacterial DAP epimerase is essential for catalysis. *J. Biol. Chem.* **288,** 9238–9248
17. Brand, I. L., Civciristov, S., Taylor, N. L., Talbo, G. H., Pantaki-Eimany, D., Levina, V., Clem, R. J., Perugini, M. A., Kvansakul, M., and Hawkins, C. J. (2012) Caspase inhibitors of the P35 family are more active when purified from yeast than bacteria. *PLoS ONE* **7,** e39248
18. Atkinson, S. C., Dogovski, C., Downton, M. T., Pearce, F. G., Reboul, C. F., Buckle, A. M., Gerrard, J. A., Dobson, R. C., Wagner, J., and Perugini, M. A. (2012) Crystal, solution and *in silico* structural studies of dihydrodipicolinate synthase from the common grapevine. *PLoS ONE* **7,** e38318
19. Atkinson, S. C., Dogovski, C., Downton, M. T., Czabotar, P. E., Dobson, R. C., Gerrard, J. A., Wagner, J., and Perugini, M. A. (2013) Structural, kinetic and computational investigation of *Vitis vinifera* DHDPS reveals new insight into the mechanism of lysine-mediated allosteric inhibition. *Plant Mol. Biol.* **81,** 431–446
20. Voss, J. E., Scally, S. W., Taylor, N. L., Atkinson, S. C., Griffin, M. D., Hutton, C. A., Parker, M. W., Alderton, M. R., Gerrard, J. A., Dobson, R. C., Dogovski, C., and Perugini, M. A. (2010) Substrate-mediated stabilization of a tetrameric drug target reveals achilles heel in anthrax. *J. Biol. Chem.* **285,** 5188–5195
21. Sreerama, N., and Woody, R. W. (2000) Estimation of protein secondary structure from circular dichroism spectra: comparison of CONTIN, SELCON, and CDSSTR methods with an expanded reference set. *Anal. Biochem.* **287,** 252–260
22. Atkinson, S. C., Hor, L., Dogovski, C., Dobson, R. C., and Perugini, M. A. (2014) Identification of the *bona fide* DHDPS from a common plant pathogen. *Proteins* **82,** 1869–1883
23. Burgess, B. R., Dobson, R. C., Bailey, M. F., Atkinson, S. C., Griffin, M. D., Jameson, G. B., Parker, M. W., Gerrard, J. A., and Perugini, M. A. (2008) Structure and evolution of a novel dimeric enzyme from a clinically-important bacterial pathogen. *J. Biol. Chem.* **283,** 27598–27603
24. Laue, T. M., Shah, B. D., Ridgeway, T. M., and Pelletier, S. L. (1992) in *Analytical Ultracentrifugation in Biochemistry and Polymer Science*, pp. 90–125, The Royal Society of Chemistry, Cambridge, United Kingdom
25. Schuck, P. (2000) Size-distribution analysis of macromolecules by sedimentation velocity ultracentrifugation and Lamm equation modeling. *Biophys. J.* **78,** 1606–1619
26. Schuck, P., Perugini, M. A., Gonzales, N. R., Howlett, G. J., and Schubert, D. (2002) Size-distribution analysis of proteins by analytical ultracentrifugation: strategies and application to model systems. *Biophys. J.* **82,** 1096–1111
27. Vistica, J., Dam, J., Balbo, A., Yikilmaz, E., Mariuzza, R. A., Rouault, P. A., and Schuck, P. (2004) Sedimentation equilibrium analysis of protein interactions with global implicit mass conservation constraints and systematic noise decomposition. *Anal. Biochem.* **326,** 234–256
28. Konarev, P. V., Volkov, V. V., Sokolova, A. V., Koch, M. H. J., and Svergun, D. I. (2003) PRIMUS: a Windows-PC based system for small-angle scattering data analysis. *J. Appl. Crystallogr.* **36,** 1277–1282
29. Petoukhov, M. V., Konarev, P. V., Kikhney, A. G., and Svergun, D. I. (2007) ATSAS 2.1: towards automated and web-supported small-angle scattering data analysis. *J. Appl. Crystallogr.* **40,** s223–s228
30. Svergun, D. I. (1992) Determination of the regularization parameter in indirect-transform methods using perceptual criteria. *J. Appl. Crystallogr.* **25,** 495–503
31. Mertens, H. D. T., and Svergun, D. I. (2010) Structural characterization of proteins and complexes using small-angle x-ray solution scattering. *J. Struct. Biol.* **172,** 128–141
32. Svergun, D. I., Barberato, C., and Koch, M. H. J. (1995) CRYSOL: a program to evaluate x-ray solution scattering of biological macromolecules from atomic coordinates. *J. Appl. Crystallogr.* **28,** 768–773
33. Svergun, D. I. (1999) Restoring low resolution structure of biological macromolecules from solution scattering using simulated annealing. *Biophys. J.* **76,** 2879–2886
34. Krissinel E., and Henrick, K. (2007) Inference of macromolecular assemblies from crystalline state. *J. Mol. Biol.* **372,** 774–797
35. Dogovski, C., Gorman, M. A., Ketaren, N. E., Praszkier, J., Zammit, L. M., Mertens, H. D., Bryant, G., Yang, J., Griffin, M. D., Pearce, F. G., Gerrard, J. A., Jameson, G. B., Parker, M. W., Robins-Browne, R. M., and Perugini, M. A. (2013) From knock-out phenotype to three-dimensional structure of a promising antibiotic target from *Streptococcus pneumoniae*. *PLoS ONE* **8,** e83419
36. Laber, B., and Amrhein, N. (1989) A spectrophotometric assay for *meso*-diaminopimelate decarboxylase and L-α-amino-ε-caprolactam hydrolase. *Anal. Biochem.* **181,** 297–301
37. Myers, D. P., Jackson, L. K., Ipe, V. G., Murphy, G. E., and Phillips, M. A. (2001) Long-range interactions in the dimer interface of ornithine decarboxylase are important for enzyme function. *Biochemistry* **40,** 13230–13236
38. Coleman, C. S., Stanley, B. A., and Pegg, A. E. (1993) Effect of mutations at active site residues on the activity of ornithine decarboxylase and its inhibition by active site-directed irreversible inhibitors. *J. Biol. Chem.* **268,** 24572–24579
39. Tsirka, S., and Coffino, P. (1992) Dominant negative mutants of ornithine decarboxylase. *J. Biol. Chem.* **267,** 23057–23062
40. Soares da Costa, T. P., Christensen, J. B., Desbois, S., Gordon, S. E., Gupta, R., Hogan, C. J., Nelson, T. G., Downton, M. T., Gardhi, C. K., Abbott, B. M., Wagner, J., Panjikar, S., Perugini, M. A. (2015) Quaternary structure

analyses of an essential oligomeric enzyme. *Methods Enzymol.* **562,** 205–223
41. Renatus, M., Stennicke, H. R., Scott, F. L., Liddington, R. C., and Salvesen, G. S. (2001) Dimer formation drives the activation of the cell death protease caspase 9. *Proc. Natl. Acad. Sci. U.S.A.* **98,** 14250–14255
42. Ali, M. H., and Imperiali, B. (2005) Protein oligomerization: how and why. *Bioorg. Med. Chem.* **13,** 5013–5020
43. Gerrard, J. A., Hutton, C. A., and Perugini, M. A. (2007) Inhibiting protein-protein interactions as an emerging paradigm for drug discovery. *Mini Rev. Med. Chem.* **7,** 151–157
44. Wells, J. A., and McClendon, C. L. (2007) Reaching for high-hanging fruit in drug discovery at protein–protein interfaces. *Nature* **450,** 1001–1009
45. Merabet, N., Dumond, J., Collinet, B., Van Baelinghem, L., Boggetto, N., Ongeri, S., Ressad, F., Reboud-Ravaux, M., and Sicsic, S. (2004) New constrained "molecular tongs" designed to dissociate HIV-1 protease dimer. *J. Med. Chem.* **47,** 6392–6400